RESEARCH ARTICLE | SEPTEMBER 20 2022

Instrument for *in situ* study of rolling under normal load and torque ⊘

Milosz K. Rajchel; Michael Varenberg; Michael J. Leamy ⓘ ; Antonia Antoniou ✉ ⓘ

Check for updates

View Online   Export Citation   CrossMark

AIP Publishing

Instrument for *in situ* study of rolling under normal load and torque

View Online   Export Citation   CrossMark

Milosz K. Rajchel, Michael Varenberg, Michael J. Leamy, (iD) and Antonia Antoniou[a] (iD)

AFFILIATIONS

The Woodruff School of Mechanical Engineering, Georgia Institute of Technology, Atlanta, Georgia 30332, USA

[a] Author to whom correspondence should be addressed: antonia.antoniou@me.gatech.edu

ABSTRACT

Instabilities that develop at the contact interface of solid rollers or airless tires while in motion can lead to increased energy losses and reduced service life. This manuscript describes an instrument that can give better insight into the origin of such instabilities by monitoring both local and global roller mechanics. This is done by simultaneously obtaining force and displacement data from sensors as well as optical measurements and local deformation fields across two different planes, extracted from images taken by a high-speed camera. Multiple loading configurations are possible, ranging from static normal loading of the roller to free rolling and rolling with a propulsive or a braking torque. Instrument functions, elements, and design are presented in detail and its capabilities are demonstrated by obtaining measurements such as width of the contact interface under normal loading, strain fields of the roller sidewall and contact interface under normal loading, and the roller's resistance to motion for free and forced rolling.

Published under an exclusive license by AIP Publishing. https://doi.org/10.1063/5.0100081

INTRODUCTION

Elastic rolling elements, such as tires and rollers, find usage in many applications in automotive, aerospace, and manufacturing industries.[1–16] Designing and optimizing rolling elements for these applications entail accurate characterization of rolling behavior including roller dynamics, deformation, and interactions between rolling elements and their counterparts. In some cases, optimization of one parameter can lead to a decrease in performance of another. For example, minimizing rolling resistance in vehicle tires leads to better energy usage while typically reducing tire traction.[1,2] Rollers used in manufacturing, such as those in printers or extrusion machines, are subject to trade-offs between strength and elastic strain recovery as well as chemical resistance and desirable frictional properties.[3] Reconciling such issues requires comprehensive knowledge of global system behavior and, in turn, calls for designing adequate experimental test rigs.

Rolling experiments generally involve the use of sensors to quantify key forces and displacements. Sensors commonly used include strain gauges, distance encoders, accelerometers, and optical sensors. Measurement methods can be split into contact[4–7] and noncontact methods.[8–13] Contact measurement methods utilize sensors to extract discrete measurements at their points of placement.

Niskanen and co-workers employed accelerometers within tire treads to measure the effects of various road conditions on the acceleration of the tire and to estimate the length of the contact patch.[5,6] While utilizing multiple sensors provides a wider measurement scope, sensor placement can affect experimental results by changing the dynamics of the system, resulting in a trade-off between resolution and accuracy. Furthermore, accelerometers and strain gauges are prone to alignment errors and suffer from reliability issues in harsh environments and high-speed or high-vibration operating conditions. Stiff sensors, such as strain gauges, adhered to elastic surfaces can delaminate from the surfaces during deformation.[8] Lian *et al.* developed a test rig with a single strain gauge to study an elastomeric roller's rolling resistance coefficient.[14] The use of a single strain gauge placed on the frame had minimal impact on the roller's dynamics. However, the measurements were susceptible to misalignment errors and strongly impacted by roller eccentricity. Other approaches involve the use of post-experiment noise filtering or model development and calibration methods to properly obtain information about the contact characteristics.[17,18]

Noncontact sensing methods typically utilize optical measurements provided by lasers[15,16] or cameras.[2,9–13,16,19] These methods have high accuracy, can operate in a multitude of conditions, and exhibit fewer difficulties than direct sensor placement.[8] Utilization

of cameras in rolling experiments dates as far back as 1963 when a high-speed camera was used to investigate aircraft hydroplaning.[9] For rolling elements, of interest herein, Tuononen applied a laser triangulation sensor to optically measure tire carcass deflection of a rolling tire. The instrument provided a single-point deformation measurement.[15] Matsuzaki *et al.* monitored in-plane strain and out-of-plane displacement of a rolling tire using a camera fixed on a rim.[10] The addition of the mass of a camera to a point in the tire had a direct effect on the dynamics of the wheel. Bodini *et al.* proposed a test rig utilizing a high-speed camera with multiple laser systems used to monitor wheel and rail interactions in a miniaturized lab setting. The test rig allowed for construction of a 3D profile of a deformed rail specimen from numerous 2D profiles of the specimen.[16]

A noncontact optical technique, digital image correlation (DIC), can be used to extract full-field displacement and strain fields of an object of interest by tracking the deformation of points on its surface.[20] This technique has been extensively applied to deformation measurements in static/quasi-static systems in a range of environments,[21,22] and it is recently gaining acceptance in measurements of dynamic applications such as impact of rock[23] or other granular media.[24] Mange *et al.* applied DIC to extract strain fields of a rolling tire sidewall to investigate tire vibrational characteristics.[11] Gao *et al.* extracted the strain fields of the tire sidewall to study tire deformation and contact peculiarities in a high-speed rolling condition.[12,13] Liang *et al.* employed DIC to obtain strain fields of the contact interface to study rolling resistance and traction.[2]

The rolling of an elastomeric roller on a relatively rigid surface can be closely related to the rolling of a rigid roller on an elastomeric surface. An example of the latter case is a belt drive system in which an elastomeric belt translates around a driving and driven pulley. Recent investigations by Wu *et al.* revealed the existence of instabilities previously not known to appear in belt drives, the so-called Schallamach waves.[25,26] Based on the parallel between belt drives and rollers, these waves are expected to occur in applications involving elastomeric rollers or tires as well, but they have not yet been detected. An instrument that can closely monitor the contact interface of the roller and a substrate is required to further investigate this topic.

The *in situ* rolling instrument presented in this paper is designed to overcome challenges faced by similar setups such as limited roller loading configurations, limited measurement scope and resolution, and undesirable influence of instrument elements on rolling behavior. Utilizing multiplane DIC with force and displacement measurements provided by sensors, this instrument is used to characterize rolling behavior including in-plane roller deformation, contact area evolution, frictional behavior, rolling resistance, and contact instabilities. It enables investigators to obtain simultaneous in-plane deformation maps of an elastomeric roller sidewall and contact interface with a rigid substrate as well as nonintrusive force and displacement measurements to enable new understanding of global and local rolling dynamics.

INSTRUMENT DESCRIPTION

Figure 1 represents a schematic outlining the key elements of the instrument. It can be broken down into driving, loading, and
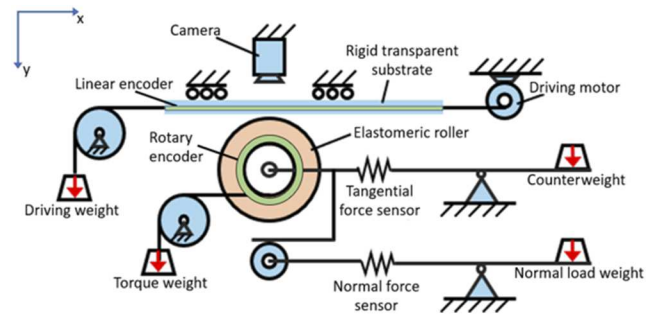

FIG. 1. Schematic of the instrument.

data acquisition systems. The driving system controls the relative motion of the wheel, consisting of an elastomeric roller and a metal hub, and the substrate. As shown, the elastomeric roller is situated below a rigid transparent substrate. The roller can spin but does not displace in the *x*-direction. Instead, the substrate located above the roller can translate along the *x*-direction, which induces rolling of the elastomeric roller. This facilitates stationary monitoring of the roller–substrate contact interface. The driving motor controls the velocity of the substrate while the driving weight provides motion stability.

The loading system applies a *y*-direction normal force as well as a propulsive or braking torque to the wheel. The ability to independently control the magnitude of the normal force and the type and magnitude of the torque applied to the wheel enables exploration of a multitude of loading conditions. The magnitude of the applied normal force and of the applied torque can be controlled by varying the mass of the normal load weight and the torque weight.

The data acquisition system captures the effects of varying operating conditions. Two force sensors and two displacement encoders provide numerical data. A high-speed camera takes images that can be used to obtain optical measurements and extract displacement and strain fields of the roller sidewall and contact interface.

To clarify the instrument's capability to quantify global wheel dynamics, we first describe dynamic loading of the wheel in contact with the substrate and discuss all pertinent loads, displacements, and deformations in the system. Figure 2 provides a schematic of the wheel as it comes into contact with the rigid substrate before the wheel begins to roll. In Fig. 2(a), the wheel has not yet contacted the substrate. Figure 2(b) depicts the system after the application of a normal load to the hub. This normal load causes the wheel to translate in the negative *y*-direction while the substrate remains fixed in space. The roller then deforms. Due to the large difference in elastic moduli of the substrate and the steel hub compared to the elastomeric roller, neither the rigid substrate nor the steel hub experiences significant deformation. We calculate the deformed wheel radius as

$$R_D = R - v_C, \tag{1}$$

where R_D denotes the deformed wheel radius, R denotes the undeformed wheel radius, and v_C denotes the *y*-direction displacement
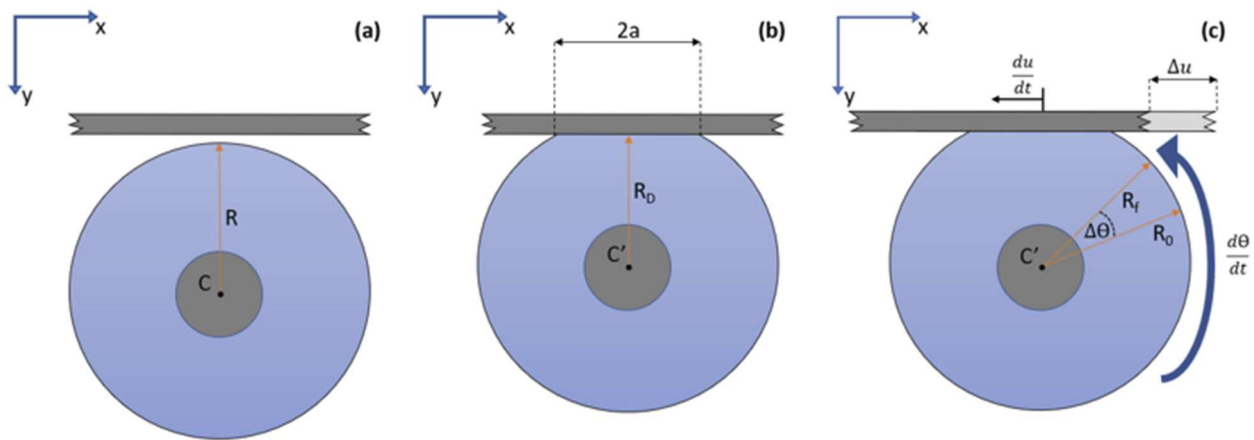
FIG. 2. Diagrams of loading stages of the wheel. (a) Wheel and substrate before contact. (b) Deformed roller after normal load is applied. (c) The system in motion.

of the center of the hub (C), also known as the normal relative displacement, after the roller contacts the substrate. Both y-direction displacement (v_C) as well as contact width (2a) can be obtained through imaging as discussed later. Figure 2(c) depicts the system in motion after the substrate has displaced by an x-direction displacement (Δu) and the roller has rotated by $\Delta \theta$ radians. We obtain Δu and $\Delta \theta$ directly through the linear and rotary displacement encoders. The difference between the distance traveled by the roller contact face and the substrate can be used to assess the degree of sliding that takes place in the system, s, as follows:

$$s \equiv R_D \times \Delta \theta - \Delta u. \qquad (2)$$

When no sliding takes place between the roller and the substrate, the distances derived from the linear and rotary encoders are equal. However, microslip always takes place in the rolling interface,[27] and gross slip occurs under a large propulsive or braking torque applied to the roller.

Figure 3 consists of four free-body diagrams that identify all forces that can act on the wheel after it contacts the substrate. The configurations explored are clockwise free rolling, counterclockwise free rolling, propulsive rolling, and braking rolling. The wheel has a radius R, a deformed radius R_D, and rotates with angular velocity ($\frac{d\theta}{dt}$). Along the y-direction, we have the user-controlled normal force applied to the wheel hub axis (N_H) and the equal but opposite normal reaction force from the substrate on the roller (N_R). We measure N_H directly with the normal force sensor. The resultant of the normal reaction force is offset by a distance (d) from the vertical axis passing through the wheel center within the contact patch length (2a). In the x-direction, we have the tangential reaction force (T_R) acting along the interface, the force measured by the tangential force sensor (T_S), and the user-controlled tangential hub force (T_H), which acts a distance (r) from the center of the wheel (C). The direction of T_R can change based on operating conditions.

Figures 3(a) and 3(b) depict clockwise and counterclockwise free rolling, respectively, with no torque applied to the wheel.

Figure 3(c) features the wheel with a propulsive torque while Fig. 3(d) depicts a wheel with a braking torque. For the propulsive case, force T_H results in a torque in the same direction as the angular velocity of the wheel, which further drives the rotation of the wheel. In the braking case, the direction of the resulting torque is opposite to the direction of the wheel's angular velocity, impeding its rotation.

Hysteretic energy losses, as well as the application of T_H during rolling, lead to the development of a torque resisting motion (TRM). In the free rolling cases, this TRM is often referred to as the moment of rolling resistance.[28] The study of rolling resistance is pertinent to any application involving rolling motion, particularly those involving elastomeric elements. We obtain an expression for TRM by taking a balance of moments about the normal projection of the wheel axis on the contact interface,

$$TRM \equiv N_R d = \mp T_S R_D \pm T_H (R_D + r). \qquad (3)$$

The upper signs correspond to the propulsive torque case and clockwise free rolling while the lower signs correspond to the braking torque case and counterclockwise free rolling. The offset (d) points in the negative x-direction for clockwise free rolling and in the positive x-direction for counterclockwise free rolling.

Figure 4 presents the computer aided design (CAD) model of the instrument used in realizing the Fig. 1 schematic. An interactive 3D model of the stage can be found in an online open access repository.[29] Figure 4(a) illustrates the positioning of the roller within the instrument and the normal loading system. The roller sits on a hub resting on bearings within the wheel holding cage, which allows the roller to rotate and displace upward along a small arc as to come into contact with the substrate above it. Placing a normal load weight on the end of the normal load lever applies force N_H to the bottom of the wheel holding cage, pressing the roller up against the substrate. Force N_H equals the weight of the normal load weight.

Figure 4(b) shows the torque-applying mechanism as well as the substrate-translating mechanism. Torque is applied by hanging
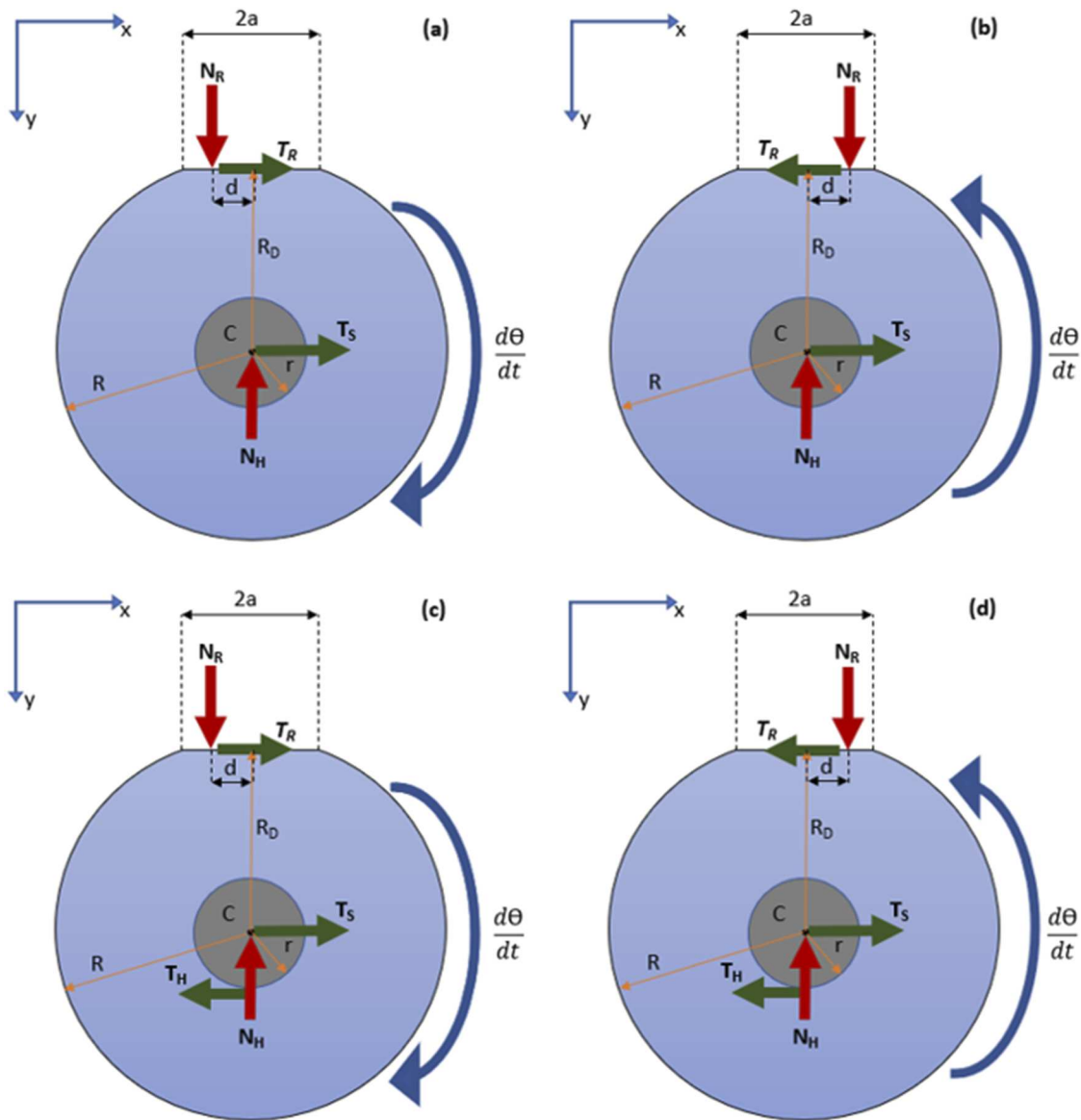
FIG. 3. Free-body diagrams of the wheel in the instrument after coming into contact with the substrate and beginning to roll. (a) Free rolling with clockwise wheel rotation. (b) Free rolling with counterclockwise wheel rotation. (c) Propulsive torque case. (d) Braking torque case.

a weight attached to a cord from the side of the instrument. The single cord splits into two cords, each of which wraps around spindles attached to both sides of the roller hub. The cord applies the tangential hub force to the wheel hub, which generates a torque about the hub center C (see Fig. 3). We can change the torque between propulsive and braking modes by changing the rolling direction of the wheel. This is accomplished by controlling the translation of the substrate. The substrate is fixed to a frame with two rails. These rails slide in a pair of linear ball bearings (SEBS 7B2-445,

Nippon Bearing Co., Ltd., Ojiya, Japan) that allow the substrate to translate relative to the wheel that rolls in place. The substrate length allows for a wheel with a 30 mm diameter to go through 3.5 rotations. The driving weight hanging off the side of the instrument is attached to one end of the substrate frame with a cord. The chord attached to the other end of the frame (not shown) winds around a spindle attached to a driving motor controlled via LabVIEW. This motor maintains a near-constant speed or any other user-specified speed profile. In the current study, the motor speed is sufficiently
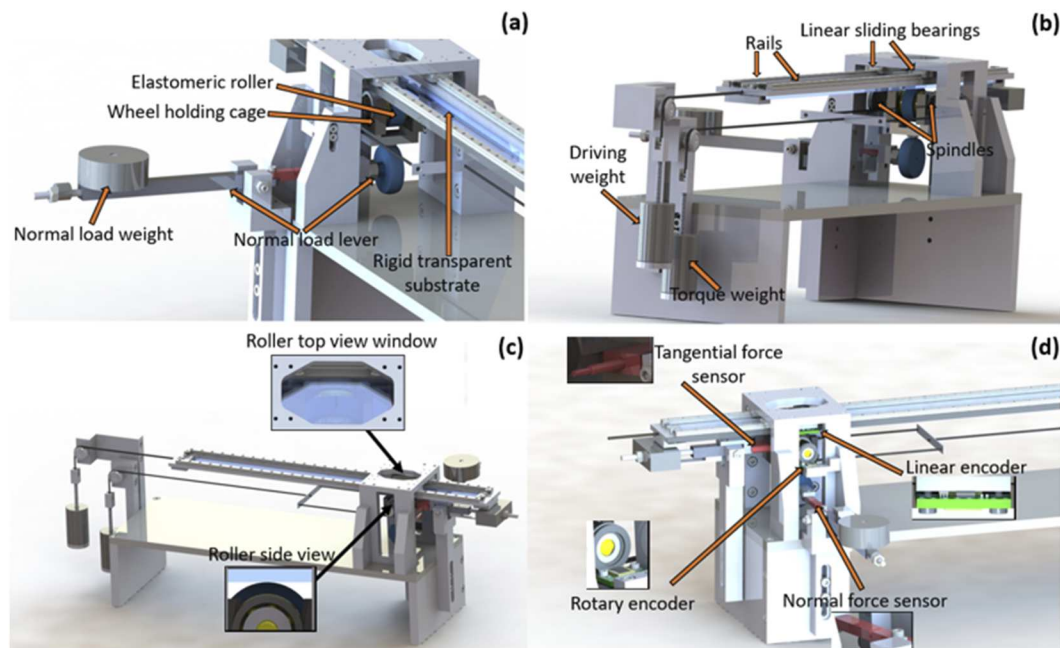
FIG. 4. (a)–(d). Four different CAD-generated views of the instrument highlighting its design and implementation.

low and the experiments are of short duration such that we assume no appreciable temperature change occurs during the rolling contact experiments.

Figure 4(c) highlights the viewing ports that allow the imaging system to capture the roller–substrate contact interface and the roller sidewall near the contact interface. The top surface of the instrument, which joins the main frame to the substrate frame, includes a large viewing window. It can be used to view and record the roller from the top through the transparent substrate. The sidewall of the roller can be viewed between the two supporting columns of the instrument.

Figure 4(d) highlights each of the four sensors located within the instrument. The normal load lever incorporates the normal force sensor (LBB200 Cantilever Bending Beam Load Cell, FUTEK, Irvine, CA), which can measure normal forces (N_H) up to 44.5 N. The x-direction force at the center of the wheel (T_S) is measured by the tangential force sensor (LSB205 JR S-Beam Load Cell 2.0, FUTEK, Irvine, CA) rated up to 44.5 N with an accuracy of ± 0.0445 N. The tangential force sensor is integrated into a lever holding the wheel holding cage. The linear encoder (RLC2IC linear encoder, RLS, Ljubljana, Slovenia) measures the linear displacement of the substrate, while the angular displacement of the wheel is measured by a rotary encoder (RLC2IC rotary encoder, RLS, Ljubljana, Slovenia). Both displacement encoders have an accuracy rating of 40 μm/m. A multifunctional data acquisition board (PCIe-6351, National Instruments Co., Austin, Texas) samples the data from the four sensors.

The force sensors used in the instrument are designed to be sensitive in order to investigate microscale instabilities expected to arise in rolling elastomeric elements.[26,30] As such, the sensors can easily

be affected by undesirable operating conditions. Ample support of the substrate frame near the substrate's interface with the roller and proper alignment of all instrument elements minimize substrate bending and y-direction displacement as well as tire/substrate misalignment, which could influence sensor readings.

The masses of the normal load weight and the torque weight shown in Fig. 4 can vary in time by adding or removing water in specially designed reservoirs. Water flows into these containers through vinyl tubes with an inner diameter of 4.3 mm from reservoirs placed ~0.5 m above the instrument. A simple valve controls the flow rate. Water can also be removed from the load containers with a pump. The ability to vary the normal load and torque in time enables investigating more loading scenarios than with the use of standard weights; for example, a torque applied to the wheel starting at zero and increasing to a max value.

Figure 5(a) displays the image acquisition system consisting of a high-speed camera (Chronos 1.4 monochrome, Kron Technologies, Vancouver, Canada) attached to a Navitar microscope lens (Navitar 12x Zoom Lens system with 1-50487 body tube, Navitar, Inc., Ottawa, Canada). The camera is positioned as to image the roller sidewall, but the same camera can be used in top view imaging. The frame acquisition rate of the camera can be configured between 20 and 1069 fps for the full resolution of 1280 × 1024 pixels^2. This enables clear images of the wheel rotating at a wide range of angular velocities. Using the minimum magnification setting of the Navitar microscope achieves a field of view (FOV) of ~15.6 × 12.5 mm^2 with a resolution of 82 pixels/mm. The maximum magnification setting yields a FOV of ~1.9 × 1.5 mm^2 and a resolution of 675 pixels/mm. Light bars (GVM 600S, GVM, San Francisco, CA) provide the required auxiliary lighting. Figure 5(b)
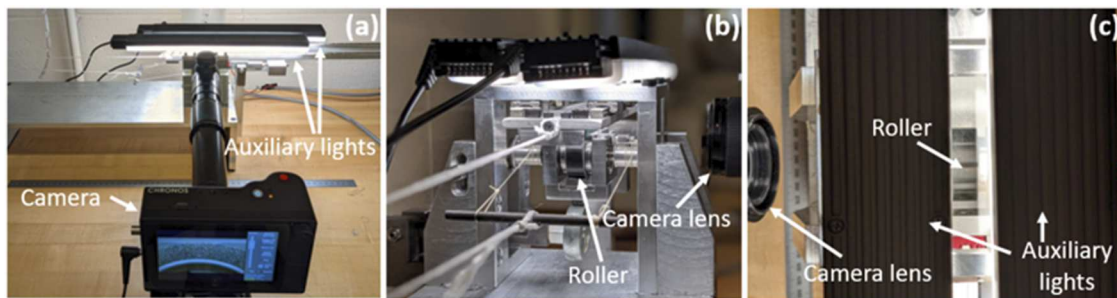
FIG. 5. Images of the instrument illustrating visual data acquisition. The black roller used has a diameter of 31 mm. (a) Instrument camera configuration used for imaging the roller sidewall. (b) Another view in which the roller is visible within the instrument. (c) The system from above; the black roller can be seen between the two auxiliary light fixtures.

shows a close up of the instrument and the camera lens in the sidewall recording configuration. Instrument elements including the roller and wheel holding cage, as well as a part of the normal force lever, are visible. Figure 5(c) shows the view of the system from above in the top viewing configuration. We can see the roller through the viewing window and the transparent substrate as the auxiliary lights provide illumination. The test rig allows for simultaneous imaging of the roller sidewall and contact interface using multiple cameras.

ROLLER FABRICATION

Figure 6 illustrates the roller fabrication. We make the roller specimens using Sylgard 184 PDMS and black paint and pattern them using spray paint. The fabrication process begins with mixing Sylgard 184 parts A and B at a 10:1 mass ratio thoroughly for 10 min. Next, we add Createx opaque black airbrush paint to this mixture at a mass ratio of 1:150 and mixed thoroughly for an additional 5 min.

The black PDMS mixture is degassed in a vacuum chamber at a pressure below 0.05 atm for 30 min in order to purge the mixture of any air bubbles. The degassed mixture is then poured into a two-part mold up to the brim as to avoid the formation of a meniscus in the final product and to achieve consistent roller geometries. We cure the full molds in an oven at 75 °C for 7 h after which we cool down the molds and carefully extract the rollers. Finally, a pattern of random speckles with an average diameter of 0.1 mm

FIG. 6. An optical image of the molds used to fabricate roller specimens.

is applied to the roller with spray paint before a heat treatment at 75 °C for an hour to further cure the speckles on the elastomer surface.

Due to the needed enhanced sensitivity of the force sensors used in the instrument, we strive to fabricate rollers with minimal eccentricity in order to minimize their impact on sensor measurements. Tangential force readings of a rotating roller exhibit noticeable cyclic behavior with the roller eccentricity as small as 50 μm (0.16% of the roller's diameter). Reducing roller eccentricity from 50 to 20 μm reduces the amplitude of cyclic oscillations in the tangential sensor readings by ~70%. Molds used in fabricating roller samples as well as the roller hub are precision machined in order to ensure minimal overall wheel eccentricity.

DEMONSTRATION OF INSTRUMENT FUNCTIONS

Figure 7 provides data from four separate initial experiments. The experiments demonstrate basic functions and illustrate how we leverage sensor and optical data to obtain measurements of wheel dynamics and deformation. Figure 7(a) shows a plot of normal load (N_H) data from the normal force sensor plotted against time. The experiment starts with a static and unloaded wheel. At t = 0, we release the normal load lever. The initial normal load applied to the wheel, ~0.6 N, is the weight of the normal load water vessel. When the fluid reservoir valve is opened at approximately t = 5, the normal load increases at a rate of ~0.2 N/s up to the final load of ~10.4 N. We present four trials of the same loading scenario to exhibit the repeatability and reliability of the loading procedure and of the sensor measurements.

Figure 7(b) presents the applied normal load (N_H) related to the normal relative displacement of the wheel (v_C). The experiment begins with a static, unloaded wheel. The high-speed camera is positioned to record the roller hub. We, then, apply a normal load to the wheel in discrete increments of about 0.5 N, progressively deforming the roller and forcing it against the substrate. The high-speed camera captures images and normal force data are recorded by the normal force sensor. We use Ncorr DIC, an open-source 2D DIC software package,[31] to extract y-direction displacement of the hub (v_C) from the images. Figure 7(b) shows the nonlinear relationship between applied load and v_C, as expected in an elastic specimen undergoing deformation.[32] Normal relative displacement
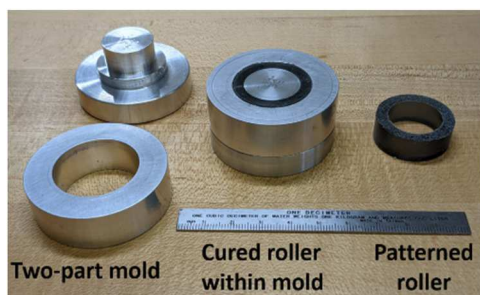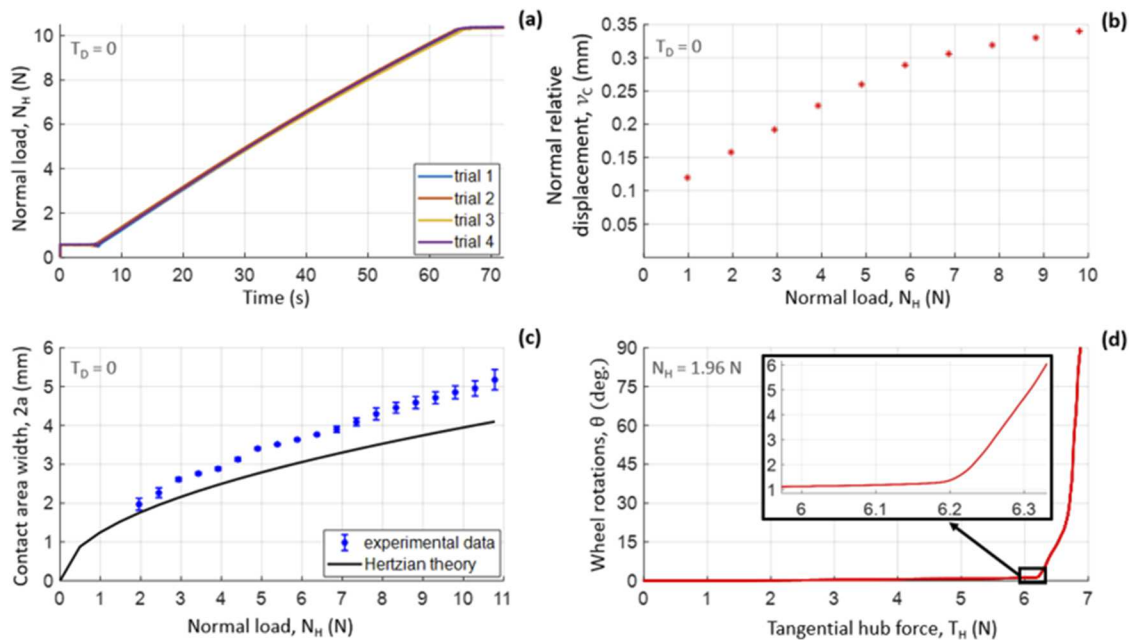
FIG. 7. Data from initial experiments with the instrument. (a) Applied normal load as a function of time. (b) Measured hub displacement as a function of load. (c) Contact area as a function of normal load. (d) Wheel rotation as a function of tangential hub force.

(v_C) is utilized as shown in Eq. (1) to find the deformed wheel radius, which is then used to calculate sliding (s), torque resisting motion (TRM), and the normal reaction force offset (d) by Eqs. (2) and (3).

Figure 7(c) explores the relationship between an applied normal load and the width of the roller–substrate contact patch (2a). The experiment starts with a static and unloaded system. The high-speed camera records the roller–substrate contact interface evolution from above. Normal loading starts at 2 N and increases in discrete increments of 5 N up to 11 N as the camera captures images of the contact interface. We measure the width of the contact patch in pixels and then convert the measurement to millimeters. The data are plotted as an average of three experimental sets with error bars equal to one standard deviation. Note that standard deviation increases for larger applied loads. The experimental data approximately match the expected contact area width as predicted by the Hertzian theory of cylinder-on-cylinder contact,[33]

$$a = 2\left(\frac{N_H}{\pi L E^*} \times \left(\frac{1}{R_1} + \frac{1}{R_2} \right)^{-1} \right)^{\frac{1}{2}}, \quad (4)$$

$$E^* = \left(\frac{1 - v_1^2}{E_1} + \frac{1 - v_2^2}{E_2} \right)^{-1}. \quad (5)$$

Equation (4) provides an estimate of the half width of the contact area of two cylinders.[34] The combined modulus of the substrate and roller, E^*, used in Eq. (4) is defined in Eq. (5). We apply it

to the case of a cylinder contacting a flat surface by considering the radius of the second cylinder to be infinite. $v_1, v_2, E_1,$ and E_2 denote the Poisson ratio and Young's modulus of the PDMS roller and tempered glass substrate, respectively. N_H and L signify the applied normal load and length of the roller. The properties of the glass and PDMS used in calculations are listed in Table I. The PDMS properties correspond to those of samples fabricated under the same curing conditions.[35,36] The substrate material is tempered glass.[37]

As seen in Fig. 7(c), Hertzian theory underestimates the contact width. In addition, Hertzian theory does not account for adhesion, which increases the contact area. This is expected since the theory assumes a homogeneous solid cylinder, while the roller used in our experiments is an anulus fitted to a metal hub. Since the metal hub experiences no significant deformation, the elastomeric roller section deforms more than a similar section of a solid elastomeric cylinder would, resulting in a larger contact area width. We observe a nonlinear relationship between applied loads and the deformation of an elastomer.

TABLE I. Properties of the PDMS roller and glass substrate used in Hertzian contact patch width calculations for Fig. 7(c).

	1 (PDMS roller)	2 (Glass substrate)
E	1.85 MPa	71.42 GPa
v	0.495	0.22

Figure 7(d) plots the rotational displacement of the wheel vs the applied tangential hub force (T_H). The experiment begins with a static and unloaded wheel. A set normal load of 2 N is applied to the wheel. Then, we apply a linearly increasing (from 0 to 7 N) tangential hub force. The wheel does not slip until the torque overcomes static friction due to 6.2 N of applied tangential hub force. At this point, the wheel grossly slips, and significant rotation is measured. The rotation of 1.4° recorded by the rotary encoder between 0 and 6.2 N of applied tangential hub force is due to elastic deformation of the roller under torque. This experiment exhibits the instrument's ability to investigate friction and stick–slip behavior.

Figure 8 shows the Lagrangian strain fields of the roller under normal loading in two different planes (side and top views). A contact patch width (2a) of 3.4 mm is marked in accordance with the maximum applied normal load of 5 N as presented in Fig. 7(c). The experiment begins with a static and unloaded wheel. A camera images the roller sidewall and contact interface as a linearly increasing normal load is applied to the wheel at an approximate rate of 0.2 N/s up to 5 N. The images are analyzed to obtain in-plane strain fields from the recorded images. Figures 8(a)–8(c) provide strain maps of the top view of the roller–substrate contact interface in the x–z plane, while Figs. 8(c), 8(d), and 8(e) provide strain maps of the roller sidewall in the x–y plane. The strain fields are shown at the maximum applied normal load of 5 N with respect to the undeformed (prior to contact) configuration. The analysis parameters correspond to a subset radius of 20 pixels (0.52 mm for the top configuration and 0.18 mm for the side configuration) with a spacing of 3 pixels (0.08 mm for the top configuration and 0.03 mm for the side configuration) and a strain radius of 20 pixels for all strain maps shown.[31] These parameters maximize the resolution of the strain fields for the given pattern.

The strain fields demonstrate complex contact behavior induced by loading. All strain fields exhibit symmetry for normal strains and antisymmetry for shear strains along the centerline of the contact patch. This is expected in a normal loading scenario with properly aligned test rig elements. No strain fields of this configuration have been published to date although a study with different operating conditions by Vu *et al.* involving contact of silicone cylinders against a glass surface produced similar interface strain fields.[38]

In Fig. 8(a), the ε_{xx} field shows purely tensile strain. It is close to zero near the region along the centerline of the contact interface. As distance from the centerline increases, ε_{xx} grows in magnitude. It reaches maximum values in two symmetric high-strain zones on either side of the interface outside of the contact patch width where the roller surface is not constrained by frictional and adhesive contact with the substrate. Roller material is pushed away from the contact zone due to the Poisson effect while the roller is compressed in the y-direction under the normal load.

The ε_{xz} field seen in Fig. 8(b) forms an antisymmetric pattern of alternating positive and negative high-strain zones separated by smaller zero-strain zones. The four central high-strain zones are roughly centered about the boundaries of the interface. Normal loading of the roller results in shearing in multiple directions away from the center of the interface. Two pairs of alternating high-strain zones form outside of the interface as well, following the same alternating pattern with a negative zone preceding or following a negative zone.

Similar to the ε_{xx} field in Fig. 8(a), the ε_{zz} field in Fig. 8(c) has the least strain in the center of the contact zone where the roller contacts and is constrained by the substrate, and it exhibits purely tensile strain. ε_{zz} grows in magnitude with radial distance away from the center of the contact zone. Unlike in the ε_{xx} field, ε_{zz} is large in magnitude near the edges of the roller sidewalls as there is no roller material there to constrain z-direction deformation.

The deformation seen in the ε_{xx} field in Fig. 8(d) is consistent with the ε_{xx} field in Fig. 8(a). There is little roller deformation in the x-direction near the surface at the contact patch due to the constrain of the roller by adhesion and friction with the substrate. However, in the center of the roller below the contact patch, ε_{xx} is greatest in magnitude. The strain is tensile near below the area near the interface and zero or slightly compressive far away from the contact patch.
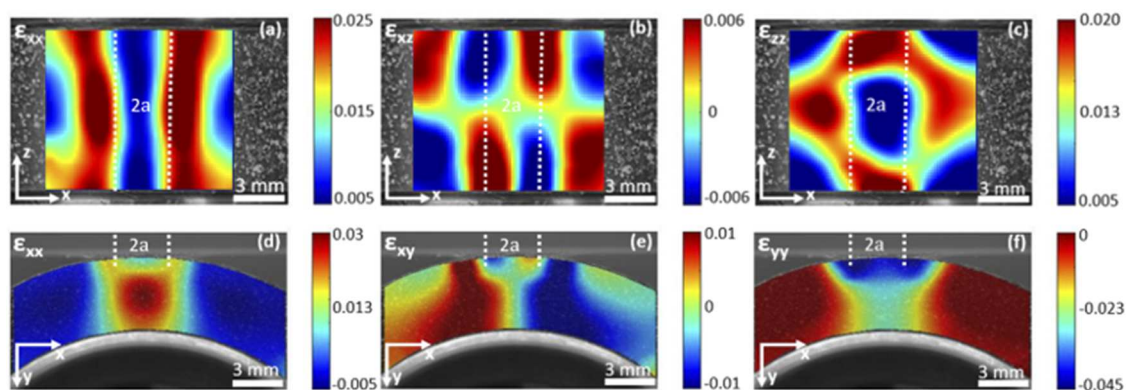
FIG. 8. Strain maps of the top and side views of the roller. During the instant shown, the wheel is subjected to 5 N normal load. Figures (a)–(c) show the top view of the contact interface, while figures (d)–(f) show the side view.
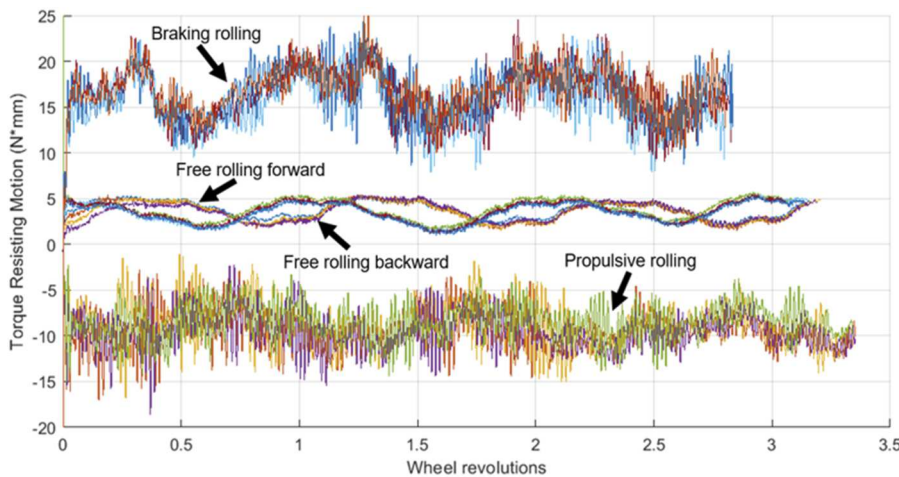
FIG. 9. TRM plots for free rolling forward, free rolling backward, the propulsive torque case, and the braking torque case. Four separate trials are plotted in different colors for each configuration.

The ε_{xy} field depicted in Fig. 8(e) forms a "fork" pattern. Shear strain is zero along a fork-like shape in the center of the roller immediately below the contact zone as well as in two areas near the top of the roller far away from the contact interface with the substrate. There is a small negative shear strain zone on the left side of the contact patch, where the roller displaces in the negative x-direction, and an antisymmetric positive shear strain zone on the right side of the contact patch, where the roller displaces in the positive x-direction. The two large antisymmetric shear strain zones that dominate the bottom of the roller near its interface with the wheel hub arise due to the same kind of deformation except on the opposite face of the roller. Deformation in the positive x-direction along the roller–hub interface results in a negative shear strain while deformation in the negative x-direction results in a positive shear strain.

As seen in Fig. 8(f), the purely compressive ε_{yy} strain field forms a "chalice" pattern with the largest magnitude strain immediately below the contact interface. The area below the contact experiences notable but lesser strain. This is because the solid wheel hub prevents further y-direction deformation. The areas far away from the contact interface on either side of the roller experience zero y-direction normal strain.

Figure 9 presents TRM [see Eq. (3)] data for four rolling configurations, each with four trials. The free rolling experiments start with a set normal load of 9.8 N. We set the substrate velocity to positive or negative 10 mm/s for the forward and backward configurations, respectively. Rolling begins from the same spot on the substrate and on the roller for all trials. We calculate TRM as shown in Eq. (3). The resulting TRM curves are consistent with each experimental configuration having a mean coefficient of variation less than 0.3.

The forward case mirrors the backward case since the only difference between the two is the direction of substrate displacement. TRM is positive for both free rolling cases, which implies it impedes the motion of the wheel, as expected. The mean magnitude of steady state TRM for the forward and backward configurations is 3.6 and 3.5 N mm, respectively. We attribute the sinusoidal behavior seen in the plots largely to the eccentricity of the roller (30 μm). As the thicker part of the roller begins to enter the contact interface, TRM increases. Conversely, as the thicker part of the roller begins to leave the contact interface, TRM decreases.

The setup of propulsive and braking rolling force experiments remains the same as the free rolling experiments except for the addition of a 9.8 N tangential hub force. The magnitude of TRM, see Eq. (3), is much larger for forced rolling cases than the free rolling cases. Sinusoidal behavior due to roller eccentricity stays present. Unlike with the free rolling cases, we observe large local oscillations in the TRM signal. This can be credited to the oscillations of the cord on which the torque weight is hung, as their oscillation frequency of 0.8 Hz aligns with calculated vibrational frequency of the cord–weight system. The average magnitude of TRM for the propulsive rolling case is −9.2 N mm while that for the braking rolling case is 16.6 N mm. We attribute the negative TRM in the propulsive rolling case to the fact that applying the tangential hub force instead of pure torque (force couple) affects reaction forces and leads to counterintuitive shifting of the offset (d), which further facilitates the motion of the wheel. For the braking rolling case, the TRM is positive, implying it impedes the motion of the wheel.

Although we use the same substrate displacement for all experiments presented in Fig. 9, the number of wheel revolutions is different for each of the rolling cases. The mean number of wheel revolutions for the free rolling cases is 3.15, while for the braking rolling and propulsive rolling cases, it is 2.83 and 3.36, respectively. This is because applying a braking or propulsive torque further deforms the roller and increases sliding at the wheel surface, so that the wheel travels shorter and longer distances in braking and propulsive rolling, respectively, when compared to its axis travel. No gross slip was observed in any of the trials depicted in Fig. 9. This suggests that the application of a torque can significantly increase the occurrence of microslip at the interface.

CONCLUSIONS

The described instrument enables investigation of contact of an elastomeric roller and a more rigid substrate under various conditions including normal loading, propulsive rolling, braking

rolling, free rolling, and sliding. Using simultaneous measurements from two force sensors, two displacement encoders, and strain and displacement maps of the interface and roller sidewall extracted with DIC, the instrument has the ability to match the evolution of the contact response and bulk deformation of the roller. The obtained data are consistent with expectations and provide insight into roller dynamics, frictional behavior, and the occurrence of contact instabilities.

ACKNOWLEDGMENTS

AUTHOR DECLARATIONS

Conflict of Interest

The authors have no conflicts of interest to disclose.

Author Contributions

Milosz K. Rajchel: Data curation (equal); Formal analysis (equal); Investigation (equal); Software (equal); Writing – original draft (equal). **Michael Varenberg**: Conceptualization (equal); Funding acquisition (equal); Methodology (equal); Supervision (equal); Writing – review & editing (equal). **Michael J. Leamy**: Conceptualization (equal); Funding acquisition (equal); Project administration (equal); Supervision (equal); Writing – review & editing (equal). **Antonia Antoniou**: Conceptualization (equal); Supervision (equal); Visualization (equal); Writing – review & editing (equal).

DATA AVAILABILITY

Data available on request from the authors.

REFERENCES

[1] J. Barrand and J. Bokar, SAE Int. J. Passenger Cars - Mech. Syst. **1**, 9 (2008).

[2] C. Liang, H. Li, H. Mousavi, G. Wang, and K. Yu, Adv. Mech. Eng. **12**, 168781402098117 (2020).

[3] W. Polston, *PFFC* (Paper, Film & Foil Converter, 1999).

[4] S.-J. Kim and A. R. Savkoor, Veh. Syst. Dyn. **27**, 189 (1997).

[5] A. J. Niskanen, Y. Xiong, and A. J. Tuononen, in *IEEE Intelligent Vehicles Symposium (IV)* (IEEE, Gothenburg, 2016).

[6] A. J. Niskanen and A. J. Tuononen, Veh. Syst. Dyn. **52**, 287 (2014).

[7] D. Garcia-Pozuelo, O. A. Olatunbosun, L. Romano, S. Strano, M. Terzo, A. J. Tuononen, and Y. Xiong, Veh. Syst. Dyn. **57**, 1970 (2019).

[8] Y. Xiong and X. Yang, Sens. Rev. **38**, 231 (2018).

[9] W. B. Horne and R. C. Dreher, *Phenomena of Pneumatic Tire Hydroplaning* (NASA Technical Report, 1963).

[10] R. Matsuzaki, N. Hiraoka, A. Todoroki, and Y. Mizutani, J. Solid Mech. Mater. Eng. **4**, 1496 (2010).

[11] A. Mange, J. Baqersad, V. Srivastava, and J. More, *SAE Technical Paper Series* (SAE international, 2018).

[12] X. Gao, Y. Zhuang, and S. Liu, Measurement **171**, 108830 (2021).

[13] X. Gao, Y. Xiong, W. Liu, and Y. Zhuang, Polym. Test. **99**, 107052 (2021).

[14] C. Lian, K.-H. Lee, and C.-H. Lee, J. Tribol. **139**, 051101 (2017).

[15] A. J. Tuononen, Meas. Sci. Technol. **22**, 125304 (2011).

[16] I. Bodini, G. Sansoni, M. Lancini, S. Pasinetti, and F. Docchio, Rev. Sci. Instrum. **87**, 083701 (2016).

[17] C. Li and L. Zhan, Rev. Sci. Instrum. **86**, 085102 (2015).

[18] L. Zhan, F. Ma, X. Song, H. Sun, and C. Li, Rev. Sci. Instrum. **90**, 095110 (2019).

[19] S. Hemette, J. Cayer-Barrioz, and D. Mazuyer, Rev. Sci. Instrum. **89**, 123903 (2018).

[20] T. C. Chu, W. F. Ranson, and M. A. Sutton, Exp. Mech. **25**, 232 (1985).

[21] J. Blaber, B. S. Adair, and A. Antoniou, Rev. Sci. Instrum. **86**, 035111 (2015).

[22] M. D. Novak and F. W. Zok, Rev. Sci. Instrum. **82**, 115101 (2011).

[23] W. Yao, C. Wang, K. Xia, and X. Zhang, Rev. Sci. Instrum. **92**, 034501 (2021).

[24] S. Ravindran, A. Tessema, and A. Kidane, Rev. Sci. Instrum. **87**, 036108 (2016).

[25] Y. Wu, M. Varenberg, and M. J. Leamy, J. Appl. Mech. **86**, 031002 (2019).

[26] Y. Wu, M. J. Leamy, and M. Varenberg, Tribol. Int. **119**, 354 (2018).

[27] R. D. Mindlin, J. Appl. Mech. **16**, 259–268 (1949).

[28] D. Tabor, London, Edinburgh, Dublin Philos. Mag. J. Sci. **43**, 1055 (1952).

[29] M. Rajchel, M. Leamy, and A. Antoniou, "Rolling apparatus interactive model," Figshare," Varenberg (2022) https://doi.org/10.6084/m9.figshare.19804378.v1.

[30] M. Barquins, D. Maugis, J. Blouet, and R. Courtel, Wear **51**, 375 (1978).

[31] J. Blaber, B. Adair, and A. Antoniou, Exp. Mech. **55**, 1105 (2015).

[32] B. J. Goodno and J. M. Gere, *Mechanics of Materials* (Cengage Learning, 2020).

[33] K. L. Johnson, *Contact Mechanics* (Cambridge University Press, 1985).

[34] A. O. Köhn and F. de Azevedo Silva, SN Appl. Sci. **2**, 1252 (2020).

[35] I. D. Johnston, D. K. McCluskey, C. K. L. Tan, and M. C. Tracey, J. Micromech. Microeng. **24**, 035017 (2014).

[36] A. Müller, M. Wapler, and U. Wallrabe, Soft Matter **15**, 779 (2018).

[37] S.-Y. Ryou, C.-S. Lee, I.-S. Cho, and A. Amanov, Materials **13**, 5644 (2020).

[38] T. L. Vu, J. Barés, S. Mora, and S. Nezamabadi, Exp. Mech. **59**, 453 (2019).